Turmell-Bot: A Configurable Cable-Driven Robot for Human Ankle Physical Therapy

Julio H. Vargas-Riaño, *Student, IEEE*, Óscar Agudelo-Varela, and Ángel Valera.

***Abstract*— We present the design of the Turmell-Bot, a configurable cable-driven robot for human ankle physical therapy. The simplest ankle model is the two-rotary serial chain known as the talocrural and subtalar axes. We focus on how the ankle tendons pull the mid-foot bones around the axes. We implemented a primary two-rotary mechanism analogous to the ankle joint. And by using the screw theory, we analyzed the interaction between ankle-foot tendons and joints. Then, we synthesized a cable-driven robot that considers the human ankle serial chain in the closed-loop mechanism. We incorporated a draw-wire sensor to measure the axes' position and orientation. Using axis projection on the base and platform planes, we balanced the actuators. We also computed the workspace and kinematics. Finally, we validated the robot's stability with the software MuJoCo and proposed a mechanical design.**

***Index Terms*— Biomechanics, Biomechatronics, Cable-driven, Medical robotics, Parallel robots, Rehabilitation robotics, Robot kinematics.**

I. Introduction

The most complex part of the human lower limb is the ankle joint. Also, it is the most commonly injured part of the body through different sports, followed by the knee [1]. We need devices with sensory feedback for quick recovery.

In this paper, we took inspiration from bio-mechatronics, robotics, and biomimetics, our technology readiness level is 2 (TRL 2).

The ankle joint is a complex articulation that moves through tendons to pull the ankle-foot structure. This arrangement is like a cable-driven serial chain, which inspired us to create a robot that mimics the action of the muscles and tendons in the ankle. We aim to replicate the natural motion of the human ankle for therapy and exercise. To achieve this goal, we created a reconfigurable tendon-driven system. We used draw-wire sensors for motion and force-sensitive sensors for pressure. Likewise, we used screw theory to find the force required for action on the Riemannian chart. The cables must compress the joint and cause movements similar to those produced by the tendons in the human ankle joint. Our contribution is the design of a configurable robot, then the actuators have similar forces when the ankle is in equilibrium. It is lightweight, we can use it in both limbs, and it is adjustable for different foot sizes. We emphasize the significance of constructing a device that is human-centered and takes into account ergonomic factors. Here, we consider comfort and adjustability to accommodate diverse foot sizes. In the future, we plan to research dynamics, control, and EMG signal integration. We aim to present multiple viewpoints on how physical therapy uses biomechanics, robotics, and engineering.

Submitted july 2023, this works is supported in part by the Colombian Administrative Department of Science, Technology and Innovation, (Colciencias) under the 568 Doctorate program, the Automatics and Informatics Institute (ai2) at Universitat Politècnica de València, (UPV) and the Facultad de Ciencias Básicas e Ingeniería (FCBI) at Universidad de los Llanos (Unillanos).

Julio H. Vargas-Riaño is with de Automatics and Industrial Informatics Research Institute at the Universitat Politècnica de València, Valencia, Spain (e-mail: julio_h_vargas_r@ieee.org).

Óscar Agudelo-Varela is with the Facultad de Ciencias Básicas e Ingeniería at the Univesidad de los Llanos, Villavicencio, Meta, Colombia.(e-mail: oscar.agudelo@unillanos.edu.co).

Ángel Valera is with Automatics and Industrial Informatics Research Institute at the Universitat Politècnica de València, Valencia, Spain (giuprog@isa.upv.es).

A. Ankle Rehabilitation Robotics

There are many state-of-the-art articles, literature reviews, and design considerations related to ankle rehabilitation robotics. For example, we found designs based on platforms [2], state-of-the-art techniques [3], and robot-assisted therapy [4]. We read about the state-of-the-art robot-assisted ankle neurorehabilitation and challenges reviewed in [5], we also found a mechanical design review in [6], robot-assisted techniques that were reviewed in [7], and a home-based review in [8]. Furthermore, we found anatomy-based designs regarding ankle-foot robotics considered in [9], and research progress in [10]. In general, most of the efforts are focused on parallel mechanisms, which have advantages over serial counterparts[11] and can be analyzed by using screw theory [12], [13], as is explained in modern robotics [14], [15].

B. Cable-Driven Robotics

Cable-driven parallel mechanisms have lightweight designs acting in tension against gravity or mutual tension configurations. They are reviewed in [16] and [17] and studied in [18]. A state-of-the-art is discussed in [19]. Cable-driven robots were applied to human arms [20], with Bowden guides [21] in lower-limbs [22]. The idea of attaching the shank and the foot was discussed in [23]. Additionally, wires [24] and a cable-driven ankle rehabilitation robot, were used in [25]. Such mechanisms are related to tendon-driven mechanisms [26], musculoskeletal robots, and artificial muscles.

II. Methodology

First, we revisited the ankle model from anatomy [27] and the International Society of Biomechanics (ISB)[28]. Then, we use the open-source digital model (z-anatomy)[29] to identify the bones, insertions, tendons, and muscles related to the ankle movement. We introduced the dimensions and geometrical model in a Jupyter Notebook using a SageMath 10 kernel [30]. Furthermore, we provided an online Jupyter notebook [31], and the CAD model [32], also on Figshare [33] and GitHub repository [34]. We identified that the tendons involved in ankle movement are an over-actuated bio-mechanism (two degrees-of-freedom four tendon groups). Then, we choose antagonistic tendon groups. Additionally, we identified the pressure forces from the platform against the plantar surface of the foot. Then, we drew a schematic with the tension forces between the base attached to the shank and a platform attached to the foot. We adapted the robot dimensions from [35], the proportions from [36], and the statistical data from [37].
We start the design by analyzing a simple cable-driven two-axis serial chain, which helps us to understand the reciprocal products between the cable and axis screw representations. Furthermore, we create artificial data from the ankle model using the forward kinematics computed from the product of exponentials (PoE). The data serve us to validate how to obtain the ankle model in practice from trajectory measurements obtained from a modification of the Turmell-Meter system [38]. When synthesizing the robot, we enlarged the device size to prevent cable contact with the body from the platform and base. Additionally, we analyzed the cable-driven antagonistic actuation in the perpendicular axes model and used it for the initial calibration. Afterward, we propose a method for the robot configuration, the workspace, and the statics simulation using MuJoCo 2.3.1 [39] for comparing the stability by changing the axis and tendon positions. Finally, we proposed a CAD model using SolidWorks 2022.

A. Robot Inspired on the Analysis of the Ankle Joint

The model has two rotational joints and four tendons involved in ankle movement. First, we analyzed the tension forces and then the compression forces. Finally, we propose a simplified schematic for the robot.

1) Ankle-Foot Tendon Forces: In this subsection, we study the two-axis representation and the tendon insertions in the bones at the mid-foot. Fig. 1a illustrates the main tendons from the lateral-anterior view of the right foot. As we show in Fig. 1a, the fifth metatarsal has two insertions, the peroneus tertius, with components for dorsiflexion and eversion, and the peroneus brevis, for eversion and plantarflexion. The calcaneus has the insertion of the Achilles tendon for inversion and plantarflexion. In Fig. 1b, we show the medial-bottom view of the foot, and the insertion points are between the first metatarsal and the medial cuneiform. The tibialis anterior contributes to inversion and dorsiflexion, the peroneus longus contributes to plantar flexion and eversion, and the tibialis posterior contributes to inversion and plantar flexion.

2) Foot Compression Forces: A requirement for ankle rehabilitation is security and comfort. We found that the foot has evolved to support high pressures in some regions of the plantar surface. In contrast, the dorsal skin is thin, soft, and vulnerable to external forces. From the bottom view of the foot, we note that the pressure points are involved in the subtalar and talocrural axes motion. They are projected to the triangle vertices of the plantar plane, located in the medial tubercle of the calcaneus and the first and fifth metatarsal heads, as shown in Fig. 1c. The pressure points are the projection of the triangular-shaped dome, limited by the lateral, medial-longitudinal arches, and the anterior transverse arch. These plantar contact points transmit a pressure force to the platform.

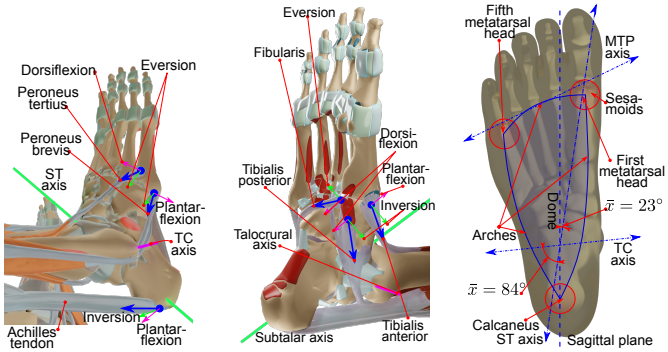

(a) Lateral top view with components tangential to each axis.

(b) Medial bottom view with components tangential to each axis.

(c) Right foots bottom plantar plane projection with contact points and joint axis.

Fig. 1: Lateral top, medial bottom, and bottom views of the ankle-foot anatomy.

3) Robot Based on the Ankle-Foot Model: The shank has a large surface, so distributing the pressure with belts and laces to fix it to the base is straightforward. The actuator cables transmit forces to the platform, which are applied pressure forces against the foot plantar surface. The cable attachment points at the base and the platform can be relocated to equilibrate antagonistic forces and adapted to different ankle axis configurations. In Fig. 2a, we sketch the approximated schematic and show the tendon directions regarding the subtalar (ST) and the talocrural (TC) axis. In Fig. 2a, we represent the foot platform with a circle with a radius r_p, centered on PM_0, and on the same plane of the anchor points ap_1, ap_2, ap_3, and ap_4. The base is a circle with a radius r_b in the same plane as P_O, and the anchor points ab_1, ab_2, ab_3, and ab_4. We simplified the plantar surface of the foot with three contact points fs_1, fs_2, and fs_3. Finally, T_1, T_2, T_3 and T_4 are tendons. The serial kinematic chain is RR, starting at the origin P_O, followed by a rotational joint at r_1 on the TC axis, followed by the $r_1 - r_2$ link to a rotational joint at r_2 on the ST axis. A link from r_2 to PM_0 connects the platform with the ankle. The tendons from ap_1, ap_2, ap_3, and ap_4 on the platform to the corresponding ab_1, ab_2, ab_3, and ab_4 on the platform complete the parallel closed-loop structure. Each human ankle has different axis positions; thus, we propose reconfigurable cable attachments, as shown in Fig. 2b.

In Fig. 2b, the green arrows illustrate the concept of recon-

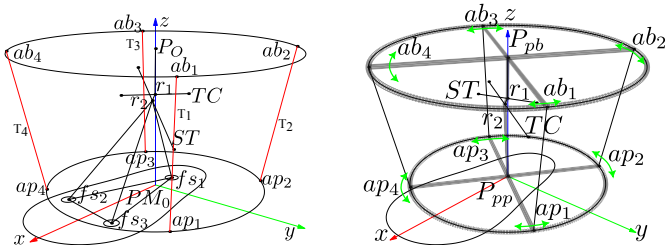

(a) Schematic representation of the approximated tendon directions in neutral position.

(b) Schematic representation of reconfiguration.

Fig. 2: Ankle model and ankle rehabilitation robot sketch.

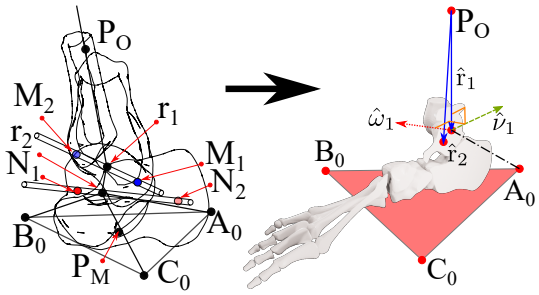

Fig. 3: Product of exponentials representation of the ankle joint.

figuration for the right foot by displacing the anchor endpoints ap_1, ap_2, ap_3, and ap_4 on the platform and the anchors ab_1, ab_2, ab_3, and ab_4 on the base. We designed a mechanism for centering pivot points P_{pb} and P_{pp}. We computed the center points from the intersection of the talocrural and subtalar axes projected on the transverse plane parallel to the base and the platform. Such pivot points are not the same as P_0 and PM_0, which pertain to the position sensors reference system.

4) Dimensions and Initial Configuration: In this section, we estimate the initial robot size and configuration. We use the ankle model and measurements from [35], human proportions from [36] and statistical data from [37]. The TC axis is dominant, and we use its statistical value for the cable-body collision analysis. We simplified the body as a sphere centered in half of the ankle's most medial point (MMP) and most lateral point (MLP); between the two malleoli. We compare this dimension with a leg model, illustrating the distance between the ankle and PM on the platform. Additionally, we show that the cables must not be in contact with the foot or the malleolus. The sphere represents the radius between the ankle and the plantar surface of the foot.

B. Ankle Representation

For the ankle kinematics representation, we used data from a two-axis model representation of the ankle joint explained in [38]. There, we described a system for platform pose capture and a method for model approximation using circle fitting.

The points M_1, M_2, and r_1 are references on the talocrural axis. Similarly, N_1, N_2, and r_2 are in the subtalar axis. We used it to compute the following vectors and matrices:

$$\hat{r_1} = r_1 - P_O, \quad \hat{r_2} = r_2 - P_O \tag{1}$$

$$\hat{\omega}_1 = \frac{M_2 - M_1}{\|M_2 - M_1\|}, \quad \hat{\omega}_2 = \frac{N_2 - N_1}{\|N_2 - N_1\|} \tag{2}$$

$$\hat{\nu}_1 = -\hat{\omega}_1 \times \hat{r}_1, \quad \hat{\nu}_2 = -\hat{\omega}_2 \times \hat{r}_2 \tag{3}$$

$$\hat{\omega}_1 = (\omega_{1x}, \omega_{1y}, \omega_{1z}), \Omega_1 = \begin{bmatrix} 0 & -\omega_{1z} & \omega_{1y} \\ \omega_{1z} & 0 & -\omega_{1x} \\ -\omega_{1y} & \omega_{1x} & 0 \end{bmatrix} \tag{4}$$

$$\hat{\omega}_2 = (\omega_{2x}, \omega_{2y}, \omega_{2z}), \Omega_2 = \begin{bmatrix} 0 & -\omega_{2z} & \omega_{2y} \\ \omega_{2z} & 0 & -\omega_{2x} \\ -\omega_{2y} & \omega_{2x} & 0 \end{bmatrix} \tag{5}$$

$$\xi_1 = \begin{pmatrix} \hat{\nu}_1 \\ \hat{\omega}_1 \end{pmatrix}, \quad \xi_2 = \begin{pmatrix} \hat{\nu}_2 \\ \hat{\omega}_2 \end{pmatrix} \tag{6}$$

Then, we compute the Rodrigues' formulas:

$$e^{\hat{\omega}_1 \theta_1} = I_{3\times3} + \Omega_1 \theta_2 + \Omega_1^2 (1 - \cos\theta_1) \tag{7}$$

$$e^{\hat{\omega}_2 \theta_2} = I_{3\times3} + \Omega_2 \theta_2 + \Omega_2^2 (1 - \cos\theta_2) \tag{8}$$

representing the θ_1 and θ_2 rotations about $\hat{\omega}_1$ and $\hat{\omega}_2$, respectively. Also, we compute the matrices:

$$e^{\hat{\xi}_1 \theta_1} = \begin{bmatrix} e^{\hat{\omega}_1 \theta_1} & \hat{\tau}_1 \\ 0_{1\times3} & 1 \end{bmatrix}, \quad e^{\hat{\xi}_2 \theta_2} = \begin{bmatrix} e^{\hat{\omega}_2 \theta_2} & \hat{\tau}_2 \\ 0_{1\times3} & 1 \end{bmatrix} \tag{9}$$

where:

$$\hat{\tau}_1 = \left(I_{3\times3} - e^{\hat{\omega}_1 \theta_1}\right) \hat{\omega}_1 \times \hat{\nu}_1 + \hat{\omega}_1 \cdot \hat{\omega}_1^T \hat{\nu}_1 \theta_1 \tag{10}$$

$$\hat{\tau}_2 = \left(I_{3\times3} - e^{\hat{\omega}_2 \theta_2}\right) \hat{\omega}_2 \times \hat{\nu}_2 + \hat{\omega}_2 \cdot \hat{\omega}_2^T \hat{\nu}_2 \theta_2 \tag{11}$$

If we define the initial pose representation as:

$$g_P(0) = \begin{bmatrix} R_0 & P_0 \\ 0_{1\times3} & 1 \end{bmatrix} \tag{12}$$

where:

$$R_0 = [\hat{s}_0 \quad \hat{n}_0 \quad \hat{a}_0] \tag{13}$$

where each column vector is:

$$\hat{s}_0 = \frac{B_0 + C_0 - 2A_0}{\|B_0 + C_0 - 2A_0\|} \tag{14}$$

$$\hat{n}_0 = \frac{(B_0 - A_0) \times (C_0 - A_0)}{\|(B_0 - A_0) \times (C_0 - A_0)\|} \tag{15}$$

$$\hat{a}_0 = \hat{s}_0 \times \hat{n}_0 \tag{16}$$

Then, we finally get the product of exponentials (PoE) representation for the serial chain with two hinge joints for all the P points on the platform:

$$g_P = e^{\hat{\xi}_1 \theta_1} e^{\hat{\xi}_2 \theta_2} g_P(0) = \begin{bmatrix} R_T & \tau_T \\ 0_{1\times3} & 1 \end{bmatrix} \tag{17}$$

where R_T is the total rotation matrix and τ_T is the total translation vector.

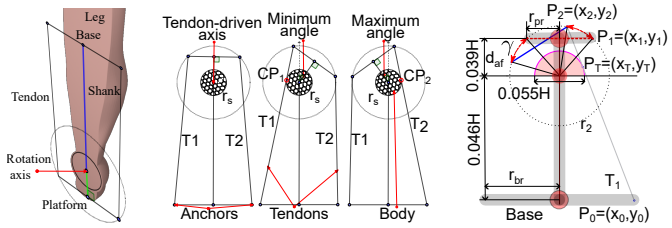

(a) Leg coronal section. (b) Collision, range of motion, and antagonistic actuation. (c) Maximum displacement.

Fig. 4: Base and platform sizes initial approximation.

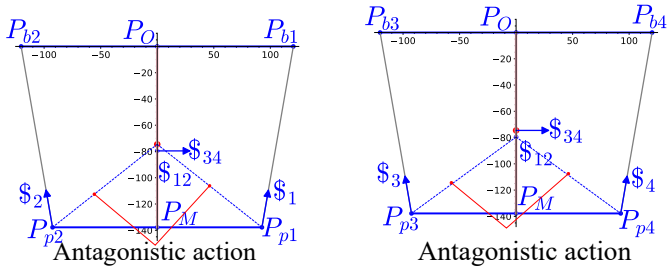

(a) Normal view to the proximal axis. (b) Normal view to the distal axis.

Fig. 5: Normal views of the proximal and distal axis regarding the base.

C. Synthesis of the Parallel Tendon-Driven Robot

The platform and base must be such that the cables must not be in contact with the body. Additionally, they must be smaller than the base and platform used by the draw-wire sensors. To simplify the collision study, we analyzed a coronal section of the foot and ankle, and the contact body is a circle containing the ankle, as illustrated in Fig. 4a. We use this coronal section to approximate the platform and base sizes. In Fig. 4b, two tendons drive a hinge joint, and the platform anchor points trace two concentric circular trajectories. The segments T_1 and T_2 represent two antagonistic tendons, r_s is the radius of a solid body containing the axis of rotation, and the interior circle represents a solid body. The collision contact of the cable with the circle depends on the base and platform proportions and the radius r_s. By observing, we note that if the base is larger than the platform, then we can enhance the range of movement of the hinge joint. The points M_1, M_2, and r_1 are references on the talocrural axis. Similarly, N_1, N_2, and r_2 are in the subtalar axis. We used it to compute the following vectors and matrices:

We use this coronal section to approximate the platform and base sizes. From the initial position, we define a maximum and minimum reached angle. In Fig. 4c, we illustrate the full range of motion of the platform. The limits are due to collision between the cables and the base body. When T_1 is extending and T_2 is contracting, Tendon T_1 touches the foot in CP_1. The minimum angle is limited for such a collision. The maximum angle occurs when T_1 is contracting and T_2 is extending. We select a radius r_s greater than the foot width, and then we evaluate a platform radius r_p greater than the radius. By selecting a base radius r_b, we can evaluate the range of movement. The positive arc and its derivate are:

$$y = \sqrt{r_s^2 - x^2} \tag{18}$$

$$\frac{\partial y}{\partial x} = \frac{-x}{\sqrt{r_s^2 - x^2}} \tag{19}$$

The derivative is the slope of the line T_1 in the tangent point P_T:

$$\frac{-x}{\sqrt{r_s^2 - x^2}} = \frac{y - y_0}{x - x_0}, \tag{20}$$

solving for y yields:

$$y = -\frac{x^2 - x \cdot x_0 - \sqrt{r_s^2 - x^2} \cdot y_0}{\sqrt{r_s^2 - x^2}} \tag{21}$$

We found the tangential point by substituting y from Equation (18) in Equation (21) (22), and simplifying yields (23):

$$\sqrt{r_s^2 - x_T^2} = -\frac{x_T^2 - x_T \cdot x_0 - \sqrt{r_s^2 - x_T^2} \cdot y_0}{\sqrt{r_s^2 - x_T^2}} \tag{22}$$

$$x_T \cdot x_0 - (r^2 - \sqrt{r_s^2 - x_T^2} \cdot y_0) = 0 \tag{23}$$

To solve for x_T, we use the software SageMath 10.0. Then, we replace the positive value in Equation (18) to find y_T.

Finally, we found the intersection P_2 with the circular trajectory that has a radius r_2. To solve for x_2, we use the following equation:

$$\frac{y_T - y_0}{x_T - x_0}(x_2 - x_0) + y_0 = \sqrt{r_2^2 - x_2^2} \tag{24}$$

We found y_2 by replacing x_2 in Equation 18.

To find the arch length, we consider the initial position of anchor point P_1 on the platform. We use the following Equation:

$$d_{af} = \sqrt{r_2^2 - x_1^2} \tag{25}$$

where d_{af} is the length from the circle center to the platform central point and defines the trajectory radius regarding the positive semicircle. We solve for x_1 yields two values. By selecting the positive value, we obtain $y_1 = d_{af}$. The arc length is given by the absolute difference of the two corresponding angles. We computed the angles by using the Equation:

$$\gamma = |\arctan_2(y_2, x_2) - \arctan_2(y_1, x_1)| \tag{26}$$

1) Cable-driven Two-Rotational Serial Chain.: In this subsection, we study a model in three dimensions that is analogous to the ankle joint. The model uses the screws in an antagonistic configuration to achieve tension forces at the cables. In the Fig. 5a, the view is normal to the proximal axis, and the Fig. 5b shows the normal view of the distal axis.

WWe use this simplified model to compute the cable locations. Also, we can use the model for testing and calibrating the mechanism before use in humans. With the purpose of designing a reconfigurable physical model, we represent the rotational joints as axes located coincident in opposite edges on a tetrahedral structure, as shown in Fig. 6. We choose two

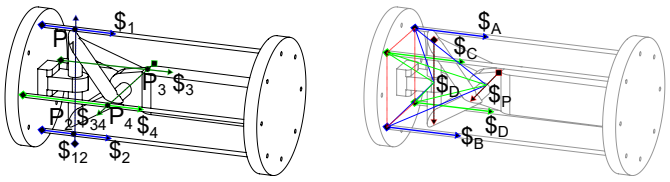

(a) Antagonistic cables screws representation.

(b) Screw representation for the anchor points rotated 45°.

Fig. 6: First approximation with orthogonal axis coplanar to the tendons.

different configurations by rotating the anchor points by 45° (half of 90°) from their initial position on the base and the platform. The first coincides with the rotation axis as in Fig. 6a, the second configuration is similar to that observed in the ankle, and we show this configuration in Fig. 6b.

The first representation allows us to visually identify the intersection points between the tendons' lines of action.

$$L_{\$_1} \cap L_{\$_{12}} = P_1, \quad L_{\$_2} \cap L_{\$_{12}} = P_2, \tag{27}$$
$$L_{\$_3} \cap L_{\$_{34}} = P_3, \quad L_{\$_4} \cap L_{\$_{34}} = P_4 \tag{28}$$

Such a condition results in null reciprocal twists because they are coplanar [40]. So the reciprocal products are:

$$\$_1 \circ \$_{12} = 0, \quad \$_2 \circ \$_{12} = 0, \tag{29}$$
$$\$_3 \circ \$_{34} = 0, \quad \$_4 \circ \$_{34} = 0 \tag{30}$$

This configuration must be avoided because it leads to a singularity.
The relations for all the tendons on the rotary joints are as follows:

$$\$_{12} \circ (\$_1 + \$_2 + \$_3 + \$_4)\,, \$_{34} \circ (\$_1 + \$_2 + \$_3 + \$_4) \tag{31}$$

In the Fig. 6a, we show the following:

$$\$_1 \circ \$_{34} = -\$_1 \circ \$_{34}, \quad \$_3 \circ \$_{12} = -\$_4 \circ \$_{12} \tag{32}$$

Then, the sum of all reciprocal products is zero, which means that the platform is in a static position. However, it is unstable because little variation in the anchor position suddenly changes the product's sign. In the second configuration, the twist pair $\$_A$ and $\$_C$ is antagonistic with regards to $\$_B$ and $\$_D$ about the proximal twist $\$_x$. Also, $\$_C$ and $\$_B$ are antagonistic with respect to $\$_A$ and $\$_D$ about the twist $\$_t$. We will use this in our design.

In summary, two conditions are important to avoid: singular configurations and cable collisions. We address the first condition by changing the angle position of the anchor points and the second condition by selecting the base and platform radiuses bigger than the foot standard size.

D. Robot Configuration

In this section, we describe the method for configuring the robot. We assume that the base plane is parallel to the transversal plane of the shank. The coordinated reference systems are aligned, and P_O and PM_0 are centered on the base and the platform, respectively. The shank line is perpendicular to the foot plane, and the neutral position occurs when the four tendons have similar tension. Therefore, the actuators used in antagonistic operation will have similar power, and the range of motion is symmetrical. When the platform of the foot is parallel to the transversal plane of the shank, the talocrural and subtalar axes projected to the plane in symmetric form are as follows:

$$\frac{x - r_{1x}}{\omega_{1x}} = \frac{y - r_{1y}}{\omega_{1y}}, \quad \frac{x - r_{2x}}{\omega_{2x}} = \frac{y - r_{2y}}{\omega_{2y}} \tag{33}$$

Solving for y yields:

$$y = \frac{\omega_{1y}}{\omega_{1x}} x - \frac{\omega_{1y}}{\omega_{1x}} r_{1x} + \frac{r_{1y}}{\omega_{1y}} \tag{34}$$
$$y = \frac{\omega_{2y}}{\omega_{2x}} x - \frac{\omega_{2y}}{\omega_{2x}} r_{2x} + \frac{r_{2y}}{\omega_{2y}} \tag{35}$$

Subtracting 35 from 34, we have:

$$x\left(\frac{\omega_{1y}}{\omega_{1x}} - \frac{\omega_{2y}}{\omega_{2x}}\right) - \left(\frac{\omega_{1y}}{\omega_{1x}} r_{1x} - \frac{\omega_{2y}}{\omega_{2x}} r_{2x}\right) + \frac{r_{1y}}{\omega_{1y}} - \frac{r_{2y}}{\omega_{2y}} = 0 \tag{36}$$

Solving for x yields:

$$x_p = -\frac{(\omega_{2y} r_{2x} - \omega_{2x} r_{2y})\omega_{1x} + (\omega_{1x}\omega_{2x} - \omega_{1y}\omega_{2x}) r_{1x}}{\omega_{1y}\omega_{2x} - \omega_{1x}\omega_{2y}} \tag{37}$$

Replacing x in 33 and solving for y yields:

$$y_p = -\frac{(\omega_{2y} r_{2x} - \omega_{2x} r_{2y})\omega_{1y} + (\omega_{1x}\omega_{2y} - \omega_{1y}\omega_{2y}) r_{1x}}{\omega_{1y}\omega_{2x} - \omega_{1x}\omega_{2y}} \tag{38}$$

We create two planes parallel to the z-axis, coincident with the intersecting point $P_{ip} = (x_p, y_p)$:

$$\Pi_1 : (P - P_{ip}) \cdot \hat{n}_{1\|z} = 0, \quad \Pi_2 : (P - P_{ip}) \cdot \hat{n}_{2\|z} = 0 \tag{39}$$

where the normal vectors are:

$$\hat{n}_{1\|z} = \hat{\omega}_1 \times [0, 0, 1], \quad \hat{n}_{2\|z} = \hat{\omega}_2 \times [0, 0, 1] \tag{40}$$

We compute the angle between the planes. This equation can be used to calculate the minimum and maximum angles, and the angles can be obtained as follows:

$$\gamma_{12} = \frac{1}{2} \arccos\left(\frac{\hat{n}_{1\|z} \cdot \hat{n}_{2\|z}}{|n_1||n_2|}\right), \tag{41}$$
$$\gamma_{21} = \frac{1}{2}\left[\pi - \arccos\left(\frac{\hat{n}_{1\|z} \cdot \hat{n}_{2\|z}}{|n_1||n_2|}\right)\right] \tag{42}$$

We rotate the unitary vector normal to the planes γ_{12} and γ_{21} about an axis parallel to the z-axis and pass it through P_{ip}. The resulting vectors are:

$$\omega_{12} = \text{rot}(\hat{k}, -\gamma_{12}), \quad \omega_{21} = \text{rot}(\hat{k}, -\gamma_{21}) \tag{43}$$

where $\hat{k}$ is the unitary vector in the direction of the positive z-axis.

The resulting lines in symmetric form are:

$$\frac{x - x_p}{\omega_{12x}} = \frac{y - y_p}{\omega_{12y}}, \quad \frac{x - x_p}{\omega_{21x}} = \frac{y - y_p}{\omega_{21y}} \tag{44}$$

Then, we obtain the pivot point $P_{pp} = [x_{pp}, y_{pp}, z_{pp}]$ on the robot platform, and the pivot point $P_{pb} = [x_{pb}, y_{pb}, z_{pb}]$ on the base, corresponding to $[x_p, y_p]$ projected on the platform and the base. The platform and base attachment points are at the intersection between the circle centered on the pivot points P_{pp} and P_{pb} with the lines of Equations 44, the circle equations are:

$$y^2 = r_p^2 - (x - x_{pp})^2 + y_{pp}, \quad y^2 = r_b^2 - (x - x_{pb})^2 + y_{pb} \tag{45}$$

The platform radius is r_p, and the base radius is r_b. By solving for y in 44, substituting it in 45, and solving for x, we can obtain the following two values:

$$\frac{\sigma \mp \sqrt{\left(\omega_{12x}^2 + \omega_{12y}^2\right)\left(y_{pp} + r_p^2\right) - \omega_{12x}^2 y_{pp}^2}}{\omega_{12x}^2 + \omega_{12y}^2} \tag{46}$$

where:

$$\sigma = \left(\omega_{12x}^2 + \omega_{12y}^2\right) x_{pp} - \omega_{12x}\omega_{12y} y_{pp} \tag{47}$$

Substituting these values back into Equation 44 yields:

$$y_{ap_1,ap_2} = y_{pp} - \frac{\omega_{12y}}{\omega_{12x}}\left(x_{pp} - x_{ap_1,ap_2}\right) \tag{48}$$

Then, by substituting ω_{12} by ω_{21}, we can obtain the other two points. Finally, we obtained four points for the platform. Obtaining the base anchor points is similar to computing the platform anchor points, replacing P_{pp} by P_{bp}, and r_p by r_b we compute four base corresponding points. The reconfigurable structure is easy to set up by changing the angle position given by:

$$\theta_{pi} = \arctan(y_{ap_i}, x_{ap_i}), \quad \theta_{bi} = \arctan(y_{ab_i}, x_{ab_i}) \tag{49}$$

where θ_{pi} and θ_{bi} are the corresponding angles of each anchor point on the platform and the base related to the x direction around the intersection projected points P_{pp} and P_{bp}.

TABLE I: Base-platform ratio and range of motion

Base	$0.5r_p$	$0.6r_p$	$0.7r_p$	$0.8r_p$	$0.9r_p$	r_p
$0.8r_p$	19.17	24.69	30.02	35.10	39.90	44.40

III. Workspace From the Product of Exponentials

By knowing the platform's initial configuration, we can plot the anchor point group of movements from the product of exponential matrices by applying the equation 17 to each platform anchor point. The product of exponential matrices for each anchor point on the platform is:

$$g_{ap_i} = e^{\hat{\xi}_1\theta_1} e^{\hat{\xi}_2\theta_2} g_{ap_i}(0) = \begin{bmatrix} R_{ap_i} & \tau_{ap_i} \\ 0_{1\times 3} & 1 \end{bmatrix} \tag{50}$$

Moreover, the cable lengths can be calculated as follows:

$$l_{ci} = \|\tau_{ap_i} - ab_i\| \tag{51}$$

The range of the talocrural angle is $\theta_1 \in [-20°, 20°]$, and the subtalar angle range is $\theta_2 \in [-15°, 15°]$ The surfaces represent the group of movements for each anchor point on the platform.

A. Reconfiguration and Statics Simulation

The robot configuration depends on the ankle axis location. We compared the analogous two-axis system and the ankle biaxial model on MuJoCo 2.3.1. We used this software because it is open-source and free to use. Additionally, it is used for model-based control. We provided the XML source in [34]. The simulation process is easy, we edited the tendon lengths in the text editor and reloaded the simulation in MuJoCo 2.3.1. We stopped the simulation, we changed the hinge joint angles, then we ran the simulation with the computed tendon lengths. The simulation stops in a static position at previously computed angles.

IV. Results

A. Fitting Different Ankle Models

In this section, we select the platform, the base sizes and the location of the anchor points for mean values. We use Fig.4c and the equation (26). The body segment is proportional to the human height H=1752 mm. The robot platform and base radius are smaller than the platform and base of the draw-wire sensor system. The range of motion for different proportional values are in Table I.

For all the cases, we need at least 30° for the angle, and a proportion near the sensors or the foot is not desirable. We select a proportion of 80% from the base and platform of the draw-wire sensor system, which is sufficient for the mean height H.

TABLE II: Point positions at equilibrium

Points	$P_1,(x,y)$	$P_2,(x,y)$	$P_3,(x,y)$	$P_4,(x,y)$
Platform, z=-137.8	(65.45,65.45)	(-65.45,-65.45)	(65.45,-65.45)	(-65.45,65.45)
Base, z=0	(85.08,85.08)	(-85.08,-85.08)	(85.08,-85.08)	(-85.08,85.08)

TABLE III: Reciprocal products.

$\$_{mn} \circ \$_i$	$\$_1$	$\$_2$	$\$_3$	$\$_4$	$\sum(\$_{mn} \circ \$_i)$
$\$_{12}$	6635.7	-6635.7	6635.7	-6635.7	0
$\$_{34}$	6218.6	-6218.6	-6218.6	6218.6	0

B. Screws Algebra Results and Reciprocity.

In this subsection, we analyze the platform screws system. We use Figure 6 as a reference, and then we build a model based on the cable anchor with the platform and base. Then, we reconfigure the anchor point places to $45°$ rotation about the z unitary axis $\hat{k}$. The base and platform corresponding points are provided in the table II.

The resulting reciprocals are in table III.

We observe that in the 45 rotated configuration, each pair of cable-driven actuators works in the tensegrity mode. Additionally, it is possible to apply work from the cables in the tension to the rotation axes in the serial kinematic chain.

C. Base Design for Pivot Centering

In this subsection, we show how to align the robot at the initial projected pivot point intersection. The alignment of this point is prior to the configuration of the anchor points on the base.

In the Fig. 8, the horizontal and vertical guides have markers when the robot is centered with respect to the draw-wire sensor system. On the top-left side, we designed scales for fine alignment after patient-specific ankle-axis estimation. The pivot point depends on the anthropometric measurements; in this case, we use the standard deviation and the mean values for the common perpendicular distance Q=mean. The resultin projection points are in Table IV.

We note that by changing the different parameters, the robot has sufficient range to reconfigure the anchor points. All values are smaller than 4 mm. So the aligning system work with different axis attitudes.

D. Angle Computation of the Anchor Points

After we centered the robot around the intersection of the talocrural and subtalar axes projected on the base and initial platform planes, we configured the four cable anchor points. To do so, we use Equations (46), (47), and (48) to compute the anchor points. In this subsection, we only change the axis attitudes and then compute the anchor points relative to the axis locations. The table V shows the resulting computed data for the mean, attitude values.

From this table, we compute the angle configuration of the attaching points in table VI.

TABLE IV: Subtalar and talocrural projection points

Axis attitude	TC mean (x_p, y_p)	TC+sd (x_p, y_p)	TC-sd(x_p, y_p)
ST mean	(0.0943,-0.8973)	(-0.0162,-0.9284)	(0.2002,-0.8674)
ST+sd	(0.1286,-1.224)	(-0.0222,-1.2739)	(0.2716,-1.1767)
ST-sd	(0.2044,-1.9448)	(-0.0373 ,-2.1371)	(0.411,-1.7805)

TABLE V: Anchor point computation at initial position

Computed variables	TC Mean attitude
$(\hat{\omega}_1, \hat{\nu}_1)$	(-0.103, 0.979, 0.174, 106, 11.1, 0)
$(\hat{\omega}_2, \hat{\nu}_2)$	(0.738, 0.208, 0.642, 23.2, -84.5, 0.682)
$\phi_1(rad)$	0.70045
$\phi_1(°)$	40.13
$\phi_2(rad)$	0.87035
$\phi_2(°)$	49.87
Vector 1	(814.89, -552.28)
Vector 2	(-430.17, -634.71)
Ap1, z=-176 2	(-76.52, 51.02)
Ap2, z=-176 2	(76.72, -52.84)
Ap3, z=-176 2	(52.03, 75.71)
Ap4, z=-176 2	(-51.83, -77.53)
Ab1, z=0 2	(-99.51, 66.59)
Ab2, z=0 2	(99.70, -68.42)
Ab3, z=0 2	(67.60, 98.69)
Ab4, z=0 2	(-67.41, -100.5)

TABLE VI: Configuration angle from x direction.

Angle	α_1	α_2	α_3	α_4
Mean (rad)	2.554	-0.603	0.969	-2.16
Mean $(°)$	146.31	-34.58	55.5	-123.8

E. Workspace

The workspace is limited by the range of movement of the ankle joint. We use Equation (50) to compute the different groups of movements shown in Fig. 7a.

F. Cable Lenghts at Initial Position

We use Equation (51) to compute the cable lengths at the initial position.

The resulting lengths for the mean values are shown in the table VII.

For the initial lenghts, we draw the forward kinematics is the intersection between four spheres and the circle representing

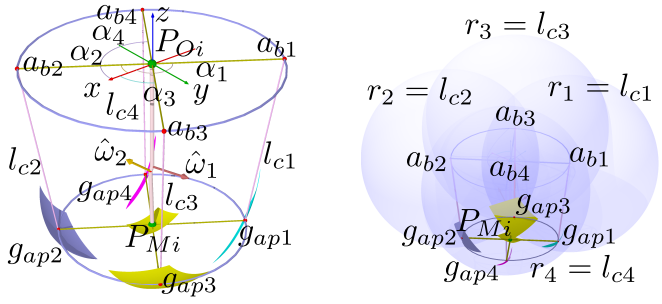

(a) Centering the platform. (b) Forward kinematics.

Fig. 7: Robot kinematics.

TABLE VII: Cable lenghts at initial position.

$(\theta_1, \theta_2), (°)$	lc_1, mm	lc_2, mm	lc_3, mm	lc_4, mm
$(0, 0)$	178.35	178.35	178.35	178.35

TABLE VIII: Rotation center r_{2i} and PM_i for extreme angles.

$(\theta_1, \theta_2), (^\circ)$	r_{2i}	P_{M_i}
$(-20, -15), (^\circ)$	(4.130, -0.2039, -110.8)	(24.31, -10.56, -170.9)
$(-20, 15), (^\circ)$	(4.130, -0.2039, -110.8)	(18.91, 13.42, -171.8)
$(20, -15), (^\circ)$	(1.361, -0.1503, -112.7)	(-19.34, -15.01, -171.7)
$(20, 15), (^\circ)$	(1.361, -0.1503, -112.7)	(-27.31, 8.175, -169.6)

TABLE IX: Anchor points ap_1, ap_2, ap_3, and ap_4 for extreme angles.

$(\theta_1, \theta_2), (^\circ)$	ap_1, mm	ap_2, mm	ap_3, mm	ap_4, mm
$(-20, -15)$	(-30.03, 55.68, 204.3)	(78.32, -78.59, -137.2)	(91.65, 50.21, 156.4)	(24.308, -10.561, -170.90)
$(-20, 15)$	(-62.04, 54.72, 185.9)	(100.3, -29.63, -157.9)	(55.68, 92.49, 142.9)	(-17.38, -67.40, -200.9)
$(20, -15)$	(-90.97, 42.28, 164.9)	(52.40, -74.07, -178.1)	(33.27, 52.65, 204.8)	(-71.83, -84.44, -138.2)
$(20, 15)$	(-103.9, 40.46, 130.3)	(49.78, -25.83, -209.4)	(8.315, 92.79, 172.7)	(-62.48, -78.16, -167.0)

the platform, with the pose represented on $g_{PM(0)}$, as in the Fig. 7b.

G. Cable Lengths at Extreme Positions

We create three tables with different axis attitudes and compute the positions. The table VIII shows r_{2_i} and P_{M_i}.

The table IX shows the anchor points ap_1, ap_2, ap_3, and ap_4.

The table X lengths for the cables.

H. Statics Simulation in Mujoco

In this section, we replace the anchor points, the kinematic chain and the tendon lengths in the XML script included in the repository [34].
In the simulation, we rotate 90 about the y-axis and scale the positions by a factor of 0.1. The units are in centimeters. The input values are in table XI.

The sensors in the print data button from Mujoco generate the MJDATA.txt file, which contains the sensor measurements. We put the sensors ouptut in table XII.

Regarding the minimum and maximum values, we stop the simulation, changing the range of the tendons and moving the joints sliders to the minimum angles.

I. Resulting Robot Design

In this subsection, we used the data captured from the ankle model and integrated the draw-wire sensors into the

TABLE X: Cable lengths lc_1, lc_2, lc_3, and lc_4 for extreme angles.

$(\theta_1, \theta_2), (^\circ)$	lc_1, mm	lc_2, mm	lc_3, mm	lc_4, mm
$(-20, -15)$	216.09	139.28	165.48	188.75
$(-20, 15)$	190.06	162.63	143.57	209.71
$(20, -15)$	166.87	184.39	212.67	139.23
$(20, 15)$	133.02	219.41	182.69	168.58

TABLE XI: Data for Mujoco.

Item	Value
Reference	0 -0.0911 17.6273
base cylinder fromto	-0.4 -0.0911 17.6273 0 -0.0911 17.6273
b1	0 6.6595 7.6668
b2	0 -6.8417 27.5878
b3	0 9.8694 24.3779
b4	0 -10.0516 10.8767
leg capsule fromto	0 -0.0911 17.6273 10.8442 -0.1037 17.6286
shnk pos	0 10.8442 -0.1037 17.6286
comp capsule fromto	10.8442 -0.1037 17.6286 11.1964 -0.0117 17.909
TC hinge pos, axis	110.8442 -0.1037 17.6286, -0.174 0.979 -0.103
b-foot capsule fromto	11.1964 -0.0117 17.909 17.6176 -0.0911 17.6273
ST hinge pos, axis	-0.0117 17.909, -0.642 0.208 0.738
ptfm cylinder fromto	17.6176 -0.0911 17.627 18.0176 -0.0911 17.6273
a-foot refpos	-10.8442 0.1037 -17.6286
p1	17.6176 5.1016 9.9653
p2	17.6176 -5.2838 25.2893
p3	17.6176 7.57 22.82
p4	17.6176 -7.753 12.4345
t1 range	17.83503 17.83513
t2 range	17.83503 17.83513
t3 range	17.83503 17.83513
t4 range	17.83503 17.83513

TABLE XII: Sensors in Mujoco.

Sensor	Measurement
Accelerometer at the platform	-0.065 -0.096 9.8
Gyro at the platform	3.4e-14 -2.7e-13 4e-14
Length tendon 1	18
Length tendon 2	18
Length tendon 3	18
Length tendon 4	18
Talocrural joint in radians	0.014
Subtalar joint in radians	0.0037

robot. The device dimensions are based on human proportions with a height of H=175 cm. The objective is to adjust the measurement device and the ankle approximated model in a configurable structure. The design is intended for the laying position. We divide the design into two main subassemblies: the platform for the foot and the base for the shank.

The resulting platform design is based on the foot anatomy by observing the Fig. 1a, 1b, and 1c. The platform is adaptable to various foot sizes based on proportions [36]. The length is also adaptable, and we show the assembly in Fig. 8a. We added a length ruler, heel support, and three force sensing resistors (FSRs). Two FSRs are used for the forefoot, and one FSR is used for the hindfoot.

To align the center of the platform to P_{pp} at the initial position. We designed perpendicular sliders, as shown in Fig. 8b.

In Fig. 8c, we show the base assembly, with sensors for ankle axis estimation. We design guides for centering the shank position P_{bp}. The anchor points are manually adjusted

TABLE XIII: Changes on tendon lenghts.

t1,t2,t3,t4, (input, cm)	Acc.(m/s^2)	Gyr.	t1,t2,t3,t4	TC(r)	ST(r)
21.6,13.92,16.54,18.87	3.4 2.5 8.8	0 0 0	21,14,17,19	-0.24	-0.34
19,16.26,14.35,20.96	2.6 -1.5 9.3	0 0 0	19,16,14,21	0.25	-0.34
16.68,18.43,21.26,13.92	-2.7 0.35 9.4	0 0 0	17,18,21,14	-0.25	0.34
13.3,21.94,18.26,16.85	-3.9 -1.4 8.9	0 0 0	13,18,18,17	0.25	0.34

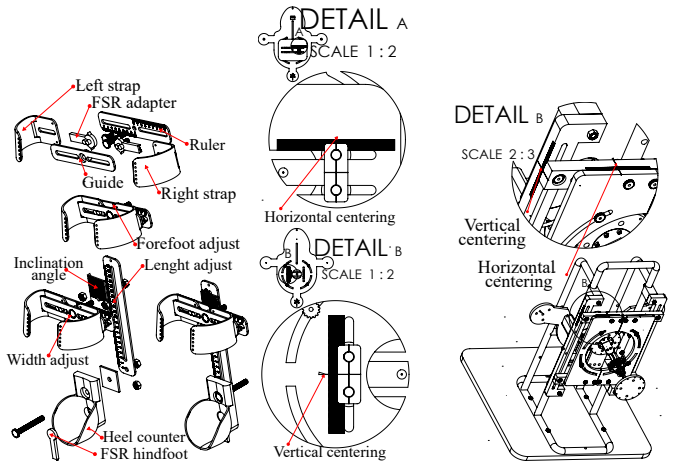

(a) Foot's size adjust. (b) Centering the platform. (c) Centering the base.

Fig. 8: Foot width, length and centering mechanisms.

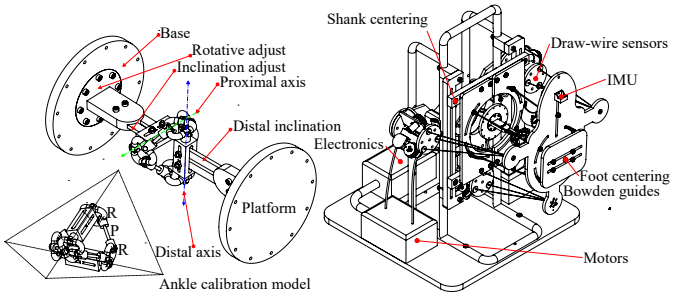

Fig. 9: CAD design.

in different positions, depending on the ankle model.

A main tube structure is attached to a baseplate. We use spacers and 8 mm steel bolts to fasten the two plates supporting the sensors. Finally, we place Bowden guides for the cable endpoints.

The final design includes the platform, the sensors, the base, and a possible configuration for the actuators and electronics. We also show a resulting assembly with the approximated adjustable axis mechanical model in Fig. 9.

V. Discussion

In this work, our results show we can use the human-centered design of an ankle rehabilitation robot for a broader group of patients following anthropometry, human proportions, and statistics. We focus on the ankle model specific to each patient to equilibrate tension and pressure forces on an initial position. For us, ankle kinematic model identification is imperative to configure the platform and base anchor points. We show that such a design can enhance the range of motion, adapting to the left and right feet and several sizes. Using this human-centered approach, we can limit the pressure forces acting on the plantar surface of the foot to avoid unnatural positions. We estimate the platform and base sizes ensuring that the cables do not touch the foot representation. The cable lengths can reach the ankle joint range of motion. The robot configuration is around the initial equilibrium position. This position is like when the human body is standing. We used projected axes on the transversal planes perpendicular to gravity. Screw theory is a powerful tool, and the results show we can effectively use it in robot geometry, kinematics, and static analysis. Using MuJoCo, we simulated the statics by editing an XML file with the computed tendon lengths and anchor points, then using sensors, the ankle joint angles measures are like the initially assumed.

VI. Conclusion

Ankle sprains are a common injury, and there is abundant research on ankle rehabilitation robots. We found that Screw Theory is applied in many works. By observing the anatomy, we realized that the tendons associated with the ankle movement are attached to the bones at the base of the plantar dome, transmitting pressure to the foot surface in contact with the platform. We designed the Turmell-Bot to be used by patients lying in bed or sitting. The robot configuration depends on the patient-specific ankle model. The model is an approximation that we can refine by using piece-wise function approximations and machine learning. We designed a lightweight, low-cost, low-energy, portable, configurable, and comfortable device. We enhance the device with sensors to measure the foot pressure forces involved in ankle movements. We will use compliant actuators and ratchets to hold the desired position without energy consumption. We will search for antagonistic actuation and tension control. We also plan to integrate electromyography (EMG) and functional electrical stimulation (FES) through the shank attachment to register the activation signals when the device is making rehabilitation movements.

Acknowledgements

Thanks to the Colombian Administrative Department of Science, Technology and Innovation, (Colciencias) under the 568 Doctorate program, the Facultad de Ciencias Básicas e ingeniería (FCBI) at the Universidad de los Llanos (Unillanos), and to the Automatics and Informatics Institute (ai2) at Universitat Politècnica de València, (UPV).

References

[1] D. T.-P. Fong, Y. Hong, L.-K. Chan, P. S.-H. Yung, and K.-M. Chan, "A systematic review on ankle injury and ankle sprain in sports:" *Sports Medicine*, vol. 37, no. 1, pp. 73–94, 2007, ISSN: 0112-1642. DOI: 10.2165/00007256-200737010-00006.

[2] Q. Miao, M. Zhang, C. Wang, and H. Li, "Towards optimal platform-based robot design for ankle rehabilitation: The state of the art and future prospects," *Journal of Healthcare Engineering*, vol. 2018, e1534247, Mar. 15, 2018, Publisher: Hindawi, ISSN: 2040-2295. DOI: 10.1155/2018/1534247.

[3] M. Dong, Y. Zhou, J. Li, *et al.*, "State of the art in parallel ankle rehabilitation robot: A systematic review," *Journal of NeuroEngineering and Rehabilitation*, vol. 18, no. 1, p. 52, Mar. 20, 2021, ISSN: 1743-0003. DOI: 10.1186/s12984-021-00845-z.

[4] A. Jahanyani, S. K. Matloub, R. K. Matloub, and S. A. H. Zahraei, "Robot-assisted therapy on ankle rehabilitation, a mini review," *Biomedical Journal of Scientific & Technical Research*, vol. 36, no. 4, pp. 28 796–28 797, Jun. 23, 2021, Company: Biomedres Distributor: Biomedres Institution: Biomedres Label: Biomedres Publisher: Biomedical Research Network+, LLC, ISSN: 2574-1241. DOI: 10.26717/BJSTR.2021.36.005894.

[5] S. Hussain, P. K. Jamwal, P. V. Vliet, and N. A. T. Brown, "Robot assisted ankle neuro-rehabilitation: State of the art and future challenges," *Expert Review of Neurotherapeutics*, vol. 21, no. 1, pp. 111–121, Jan. 2, 2021, Publisher: Taylor & Francis _eprint: https://doi.org/10.1080/14737175.2021.1847646, ISSN: 1473-7175. DOI: 10.1080/14737175.2021.1847646.

[6] Y. M. Khalid, D. Gouwanda, and S. Parasuraman, "A review on the mechanical design elements of ankle rehabilitation robot," *Proceedings of the Institution of Mechanical Engineers, Part H: Journal of Engineering in Medicine*, vol. 229, no. 6, pp. 452–463, Jun. 1, 2015, Publisher: IMECHE, ISSN: 0954-4119. DOI: 10.1177/0954411915585597.

[7] M. G. Alvarez-Perez, M. A. Garcia-Murillo, and J. J. Cervantes-Snchez, "Robot-assisted ankle rehabilitation: A review," *Disability and Rehabilitation: Assistive Technology*, vol. 15, no. 4, pp. 394–408, May 18, 2020, Publisher: Taylor & Francis _eprint: https://doi.org/10.1080/17483107.2019.1578424, ISSN: 1748-3107. DOI: 10.1080/17483107.2019.1578424.

[8] L. C. e. Chin, S. N. Basah, M. Affandi, *et al.*, "Home-based ankle rehabilitation system: Literature review and evaluation," *Jurnal Teknologi*, vol. 79, no. 6, Aug. 28, 2017, Number: 6, ISSN: 2180-3722. DOI: 10.11113/jt.v79.8468.

[9] J. Jiang, K.-M. Lee, and J. Ji, "Review of anatomy-based anklefoot robotics for mind, motor and motion recovery following stroke: Design considerations and needs," *International Journal of Intelligent Robotics and Applications*, vol. 2, no. 3, pp. 267–282, Sep. 1, 2018, ISSN: 2366-598X. DOI: 10.1007/s41315-018-0065-7.

[10] Z. Liu and D. Lu, "Research Progress of Lower Limb Rehabilitation Robots in Mainland China," en, *Open Journal of Therapy and Rehabilitation*, vol. 7, no. 3, pp. 92–105, Jun. 2019. DOI: 10.4236/ojtr.2019.73006.

[11] S. Briot and I. Bonev, "Are Parallel Robots More Accurate than Serial Robots?" *Transactions of the Canadian Society for Mechanical Engineering*, vol. 31, pp. 445–455, Nov. 2007. DOI: 10.1139/tcsme-2007-0032.

[12] Z. Liao, L. Yao, Z. Lu, and J. Zhang, "Screw theory based mathematical modeling and kinematic analysis of a novel ankle rehabilitation robot with a constrained 3-PSP mechanism topology," *International Journal of Intelligent Robotics and Applications*, vol. 2, no. 3, pp. 351–360, Sep. 1, 2018, ISSN: 2366-598X. DOI: 10.1007/s41315-018-0063-9.

[13] Q. Li and Z. Huang, "Mobility analysis of lower-mobility parallel manipulators based on screw theory," in *2003 IEEE International Conference on Robotics and Automation (Cat. No.03CH37422)*, ISSN: 1050-4729, vol. 1, Sep. 2003, 1179–1184 vol.1. DOI: 10.1109/ROBOT.2003.1241752.

[14] K. M. Lynch and F. C. Park, *Modern Robotics: Mechanics, Planning, and Control*, en. Cambridge University Press, May 2017, Google-Books-ID: OB4xDwAAQBAJ, ISBN: 9781108509695.

[15] A. Mueller, "Modern Robotics: Mechanics, Planning, and Control [Bookshelf]," *IEEE Control Systems Magazine*, vol. 39, no. 6, pp. 100–102, Dec. 2019, ISSN: 1941-000X. DOI: 10.1109/MCS.2019.2937265.

[16] C. Gosselin, "Cable-driven parallel mechanisms: State of the art and perspectives," *Mechanical Engineering Reviews*, vol. 1, no. 1, DSM0004–DSM0004, 2014. DOI: 10.1299/mer.2014dsm0004.

[17] M. Zarebidoki, J. S. Dhupia, and W. Xu, "A Review of Cable-Driven Parallel Robots: Typical Configurations, Analysis Techniques, and Control Methods," *IEEE Robotics & Automation Magazine*, vol. 29, no. 3, pp. 89–106, Sep. 2022, ISSN: 1558-223X. DOI: 10.1109/MRA.2021.3138387.

[18] A. Pott, *Cable-Driven Parallel Robots: Theory and Application*, en. Springer, Mar. 2018, Google-Books-ID: eH1TDwAAQBAJ, ISBN: 9783319761381.

[19] Z. Zhang, Z. Shao, Z. You, *et al.*, "State-of-the-art on theories and applications of cable-driven parallel robots," en, *Frontiers of Mechanical Engineering*, vol. 17, no. 3, p. 37, Sep. 2022, ISSN: 2095-0241. DOI: 10.1007/s11465-022-0693-3.

[20] M. Deman, T. Asfour, A. Ude, and A. Gams, "Mechanical design and friction modelling of a cable-driven upper-limb exoskeleton," en, *Mechanism and Machine Theory*, vol. 171, p. 104 746, May 2022, ISSN: 0094-114X. DOI: 10.1016/j.mechmachtheory.2022.104746.

[21] W. Wei, Z. Qu, W. Wang, P. Zhang, and F. Hao, "Design on the Bowden Cable-Driven Upper Limb Soft Exoskeleton," eng, *Applied Bionics and Biomechanics*, vol. 2018, p. 1 925 694, 2018, ISSN: 1176-2322. DOI: 10.1155/2018/1925694.

[22] R. Sales Gonalves, J. Carvalho, L. A. Rodrigues, and A. Marques Barbosa, *Cable-Driven Parallel Manipulator for Lower Limb Rehabilitation*. Oct. 1, 2013, vol. 459, 535 pp. DOI: 10.4028/www.scientific.net/AMM.459.535.

[23] A. Erdogan, B. Celebi, A. C. Satici, and V. Patoglu, "AssistOn-ankle: A reconfigurable ankle exoskeleton with series-elastic actuation," *Autonomous Robots*, vol. 41, no. 3, pp. 743–758, Mar. 1, 2017, ISSN: 1573-7527. DOI: 10.1007/s10514-016-9551-7.

[24] R. Yu, Y. Fang, and S. Guo, "Design and kinematic performance analysis of a cable-driven parallel mechanism for ankle rehabilitation," *Jiqiren/Robot*, vol. 37, 53–62 and 73, Jan. 1, 2015. DOI: 10.13973/j.cnki.robot.2015.0053.

[25] M. Russo and M. Ceccarelli, "Analysis of a Wearable Robotic System for Ankle Rehabilitation," en, *Machines*, vol. 8, no. 3, p. 48, Sep. 2020, ISSN: 2075-1702. DOI: 10.3390/machines8030048.

[26] R. Ozawa, H. Kobayashi, and K. Hashirii, "Analysis, Classification, and Design of Tendon-Driven Mechanisms," *IEEE Transactions on Robotics*, vol. 30, no. 2, pp. 396–410, Apr. 2014, ISSN: 1941-0468. DOI: 10.1109/TRO.2013.2287976.

[27] K. C. Ravella, J. Ahmad, and F. Amirouche, "Biomechanics of the Ankle Joint," en, in J. Koh, S. Zaffagnini, R. Kuroda, U. G. Longo, and F. Amirouche, Eds., Cham: Springer International Publishing, 2021, pp. 401–413, ISBN: 9783030815493. DOI: 10.1007/978-3-030-81549-3_31.

[28] G. Wu, S. Siegler, P. Allard, *et al.*, "ISB recommendation on definitions of joint coordinate system of various joints for the reporting of human joint motion–part I: Ankle, hip, and spine. International Society of Biomechanics," eng, *Journal of Biomechanics*, vol. 35, no. 4, pp. 543–548, Apr. 2002, ISSN: 0021-9290. DOI: 10.1016/s0021-9290(01)00222-6.

[29] K. Okubo, G. Kervyn, M. Zielinski, L. Vinent, A. T. Bigio, and C. T. Villar. "Open Source Anatomy." en. (), [Online]. Available: https://www.z-anatomy.com (visited on 05/29/2023).

[30] The Sage Developers, *Sagemath, the Sage Mathematics Software System (Version 10.0)*, https://www.sagemath.org, 2023.

[31] J. H. Vargas-Riaño. "Turmell-bot - nbviewer." (Jun. 17, 2023), [Online]. Available: https://nbviewer.org/github/juliohvr/Turmell-Bot/blob/main/TurmellBot.ipynb (visited on 06/17/2023).

[32] J. H. Vargas-Riaño. "Turmell-bot | 3d CAD model library | GrabCAD." (Jun. 17, 2023), [Online]. Available: https://grabcad.com/library/turmell-bot-1 (visited on 06/17/2023).

[33] "Turmell-bot," figshare. Publisher: figshare. (Jun. 16, 2023), [Online]. Available: https://figshare.com/articles/code/Turmell-Bot/23535756/1 (visited on 06/17/2023).

[34] J. H. Vargas-Riaño, *Juliohvr/turmell-bot: Turmell-bot*, version Turmell-Bot, Jun. 2023. DOI: 10.5281/zenodo.8051008.

[35] R. E. Isman and V. T. Inman, *Anthropometric Studies of the Human Foot and Ankle*, en. Biomechanics Laboratory, University of California, 1968, Google-Books-ID: 4Xq0GwAACAAJ.

[36] R. Drillis, R. Contini, New York University, and School of Engineering and Science, *Body segment parameters*. New York, N.Y.: New York University, School of Engineering and Science, 1966, OCLC: 22352502.

[37] C. D. Fryar, M. D. Carroll, Q. Gu, J. Afful, and C. L. Ogden, "Anthropometric reference data for children and adults: United states, 2015-2018," *Vital & Health Statistics. Series 3, Analytical and Epidemiological Studies*, no. 36, pp. 1–44, Jan. 2021, ISSN: 0886-4691.

[38] Ó. Agudelo-Varela, J. Vargas-Riaño, and Á. Valera, "Turmell-Meter: A Device for Estimating the Subtalar and Talocrural Axes of the Human Ankle Joint by Applying the Product of Exponentials Formula," en, *Bioengineering*, vol. 9, no. 5, p. 199, May 2022, ISSN: 2306-5354. DOI: 10.3390/bioengineering9050199.

[39] E. Todorov, T. Erez, and Y. Tassa, "Mujoco: A physics engine for model-based control," in *2012 IEEE/RSJ International Conference on Intelligent Robots and Systems*, IEEE, 2012, pp. 5026–5033. DOI: 10.1109/IROS.2012.6386109.

[40] J. Zhao, B. Li, X. Yang, and H. Yu, "Geometrical method to determine the reciprocal screws and applications to parallel manipulators," *Robotica*, vol. 27, no. 6, pp. 929–940, 2009. DOI: 10.1017/S0263574709005359.